Improving Wideband Massive MIMO Channel Estimation With UAV State-Space Information

Evangelos Vlachos, *Member, IEEE*, Christos Mavrokefalidis, *Member, IEEE*, Kostas Berberidis, *Senior Member, IEEE*, and George C. Alexandropoulos, *Senior Member, IEEE*

***Abstract*—In this paper, we focus on the estimation of massive Multiple-Input Multiple-Output (mMIMO) channels in high-frequency point-to-point wireless communications between a terrestrial multi-antenna base station, realizing fully digital beamforming, and a multi-antenna Unmanned Aerial Vehicle (UAV), capable of only analog combining via a single reception Radio-Frequency (RF) chain. A wideband channel model, incorporating selectivity which is usually referred to as beam squint and is particularly relevant in high frequency bands, such as millimeter waves and terahertz, is considered. To account for the UAV's limited capability to collect long training sequences, due to its single-RF reception architecture, and the beam-squint effect at both communication ends, we present a novel channel estimation approach that exploits information provided by the control module of the UAV, namely its state-space vector. The proposed approach comprises a hybrid parametric and non-parametric estimation optimization framework that is efficiently solved through an iterative algorithm using the alternating direction method of multipliers. Our extensive performance investigations, including comparisons with benchmark schemes, showcase that considerable gains can be achieved if state-space information from the UAV's control module is appropriately incorporated in the channel estimation process.**

***Index Terms*—Channel estimation, massive MIMO, UAV, THz, millimeter wave, alternating method of multipliers, state-space information.**

I. Introduction

THE integration of Unmanned Aerial Vehicles (UAVs) into wireless communications systems has been an active research area in recent years [1]. In the frame of 5G and the upcoming 6G networks and respective applications, UAVs may have a twofold role, namely, being part either of the network itself, by providing communication services as Base Stations (BSs) or relays, or of the intended application by exploiting the available communication services [2], [3], [4]. To fully exploit the capabilities of UAV-based communications, acquiring precise channel state information is crucial for optimizing various physical-layer functions such as beamforming and resource allocation. This is particularly challenging in high-frequency communication scenarios, such as millimeter-wave (mmWave) and sub-terahertz (THz) bands, especially when utilizing massive multiple-input multiple-output (mMIMO) systems [5]. However, mMIMO, when employed in the mmWave and THz ranges for utilizing larger bandwidths, raises yet another challenge related to the so-called beam-squint effect, due to measurable propagation delays manifesting along the deployed large antenna arrays [6], [7]. The above challenges lead to more elaborate channel models that require more sophisticated signal processing operations to be designed at the communication ends [8].

A. Motivation

The integration of UAVs into wireless networks capitalizes on their distinctive features and capabilities. UAVs depend on a sophisticated control module for seamless operation, overseeing and regulating crucial parameters such as the UAV's position and velocity, which are encapsulated in *state-space information* [9]. The key features and capabilities that make UAVs attractive for high-frequency mMIMO also introduce several challenges. Specifically, due to the 3D movement of UAVs, their high elevation, and the presence of water vapor at altitude, there is an increase in pathloss and attenuation, impacting signal quality and reliability over long distances. Thus, the inherent nonstationary nature of the channel, arising from UAV mobility and environmental factors, poses significant challenges for accurate and timely channel estimation. Additionally, the transceiver mounted on the UAV must be designed with limited beamforming complexity to ensure low computational and power requirements.

In this paper, the problem of estimating the high-frequency mMIMO channel between a fully digital multi-antenna BS and a multi-antenna UAV, realizing only analog combining via a single reception Radio-Frequency (RF) chain, for the case of multicarrier modulation is studied. The number of parameters to be estimated is quite large and, at the same time, due to the UAV's single-RF analog combining capability, the number of collected training sequences is short. In particular, due to the beam-squint effect, the mMIMO channel is different per subcarrier, hence, it needs to be estimated on a per-subcarrier basis. Therefore, only

Received 26 August 2024; revised 8 February 2025 and 23 April 2025; accepted 3 May 2025. Date of publication 12 May 2025; date of current version 17 October 2025. The work was supported by the EU project IoT-ECO under Grant 101083018, and project EUSOME under Grant 101187121. The review of this article was coordinated by Prof. Mugen Peng. *(Corresponding author: Evangelos Vlachos.)*

Evangelos Vlachos is with Industrial Systems Institute, ATHENA Research and Innovation Centre, 26504 Rio-Patras, Greece (e-mail: evlachos@athenarc.gr).

Christos Mavrokefalidis and Kostas Berberidis are with the Department of Computer Engineering and Informatics, University of Patras, 26504 Rio-Patras, Greece (e-mail: maurokef@ceid.upatras.gr; berberid@ceid.upatras.gr).

George C. Alexandropoulos is with the Department of Informatics and Telecommunications, National and Kapodistrian University of Athens, 15784 Athens, Greece (e-mail: alexandg@di.uoa.gr).

Digital Object Identifier 10.1109/TVT.2025.3569350

one training block is received at the UAV's baseband unit per time update for channel estimation.

To alleviate the issue of short training sequences, the proposed technique relies on the cooperation of the communication and the control modules at the UAV side. The latter feeds an estimated state vector, consisting of the UAV's position and velocity, into the communication module that then performs the estimation of the channel parameters; specifically, the spatial parameters of the Line-of-Sight (LoS) channel component and the channel matrix with the contributions of the Non-LoS (NLoS) channel paths. In this way, the additional side information used can be exploited for improving the estimation performance in view of the limited availability of training sequences.

B. Literature Review

In this context, effective channel estimation techniques are expected not only to take into account the peculiarities of the involved channels as presented previously. There exist various channel estimation techniques, whether UAVs are explicitly mentioned or implied by more general system model assumptions, that take into account the effect of beam squint, however, the involved channels have been usually assumed as time invariant. For example, [10] and [11] presented a random spatial sampling structure leading to improved channel estimation performance for cases with short training sequences, and discussed a possible extension that takes into account the beam-squint effect.

The channel estimation techniques in [12], [13], [14], [15], [16] capitalized on sparsity arguments and proposed channel estimation algorithms based on compressive sensing, off-grid sparse Bayesian learning, and block sparsity, respectively. The effect of beam squint was also tackled in [17] by considering a spectrum-based estimation algorithm which was applied on a per frequency subband basis, instead of the whole bandwidth. In [18], the proposed technique adopted a tensor-based formulation and a non-iterative solution was presented. Finally, in [19], a channel estimation algorithm for a communication link between a UAV and a reconfigurable intelligent surface [20] has been studied, however, without considering the effect of beam squint and, similarly, a sparse Bayesian approach was described in [21]. In contrast to the previous works, a channel tracking approach has been presented in [22] that employs compressive sensing arguments, however, without considering the beam squint effect. On the other hand, [23] proposed a channel estimation scheme for a UAV-based system, which considers not only the time varying nature of the involved channels but also the beam squint effect. In the same spirit, [24] presented an efficient iterative estimation algorithm for the time varying case. However, in both cases, the adopted channel model captures a single transmission path and only a multi-element antenna array at one end of the communication link was considered, which simplified considerably the requirements for the training sequences. In [25], a channel estimation technique based on tensor decomposition has been proposed for hybrid mmWave massive MIMO in high-mobility scenarios, taking into account the beam squint effect.

There are also recent works that consider the integration/collaboration of the communication system and the control module at the UAV side and present relevant channel estimation approaches. A review of the autonomous coordination and communication of swarms of UAVs is provided in [26] with a focus on applications where the UAVs are considered as end-users, like agriculture, remote sensing, and disaster management. Information available from the UAV's control module was leveraged in [27] for channel tracking in a single-UAV scenario, while [28] considered the beam-squint effect and extended the approach to trajectory design and resource allocation, among others, when multiple UAVs cooperate. Finally, a channel estimation technique that capitalizes on the knowledge of UAV's velocity, as provided by its control module, was proposed in [29]. However, in all above investigations, the adopted channel models considered only the LoS component, thus, hindering their generalization to more challenging scenarios.

C. Contributions

The contributions of this paper are summarized as follows:

- The challenge of estimating frequency selective mMIMO channels is addressed, arising from the large antenna aperture sizes and the utilization of large bandwidth at high frequencies (i.e., mmWave and THz). It is noted that the investigation of the beam-squint effect when both the transmitter and receiver sides are equipped with Uniform Planar Arrays (UPAs) has been limited in the current literature.
- A single reception RF chain is employed at the UAV side, which is selected for its reduced complexity and compatibility with most of the available UAV implementations. This limits significantly the number of the received sequences per transmission interval, as it has also been discussed in [23].
- The proposed estimation framework leverages state-space information from the UAV's control module to address the challenge of estimating under-determined channels. To address estimation errors in the state-space, a Kalman-based filter is implemented. Compared to [27], our approach presents a versatile channel model that takes into account multiple propagation paths, enhancing its applicability and robustness.
- A new hybrid optimization algorithm, combining parametric and non-parametric techniques based on the Alternating Direction Method of Multipliers (ADMM), is introduced to address the joint control and communication challenge. This approach leverages a direct two-way connection between the UAV's control module (state vector) and the communication module (channel estimation).

It is noted that this work builds upon our prior contribution [29], by: *i*) extending the problem formulation to a more general scenario including the beam-squint effect at both the UPA-equipped transmitter and receiver sides; *ii*) considering that the UAV implements analog combining with a single reception RF chains; and *iii*) adopting a more general channel capturing multiple signal propagation paths. Thus, the resulting problem

TABLE I
THE MATHEMATICAL NOTATIONS OF THIS PAPER

a, $\mathbf{a}$, and $\mathbf{A}$	Scalar, vector, and matrix
$(\cdot)^*$	The complex conjugate of the input
$j \triangleq \sqrt{-1}$	The imaginary unit
$\mathbf{A}^{\mathrm{T}}$ and $\mathbf{A}^{\mathrm{H}}$	Matrix transpose and Hermitian transpose
$\mathbf{A}^{-1}$	Matrix inverse and pseudo-inverse
$[\mathbf{a}]_i$ and $[\mathbf{A}]_{i,j}$	The i-th element of vector $\mathbf{a}$ and at the i-th row and j-th column of matrix $\mathbf{A}$
$\mathbf{I}_N$ and $\mathbf{0}_N$	$N \times N$ identity and matrix with zeros
$\times$ and $\otimes$	Scalar and Kronecker products
$\mathbb{R}$ and $\mathbb{C}$	The sets of real and complex numbers
$x \sim \mathcal{CN}(0, \sigma^2)$	x is a zero-mean complex Gaussian random variable with variance σ^2
$\mathcal{E}\{x\}$	Expectation of random variable x
$\|\cdot\|_*$, $\|\cdot\|_1$, $\|\cdot\|_2$, $\|\cdot\|_{\mathrm{F}}$	Nuclear, ℓ_1, ℓ_2, and Frobenius norms
$\mathrm{vec}(\mathbf{A})$	A function to vectorize an $M \times N$ matrix into an $MN \times 1$ vector by stacking its columns
$\mathrm{vec}^{-1}(\mathbf{A})$	The inverse operation of $\mathrm{vec}(\mathbf{A})$

becomes more challenging, leading to a novel problem formulation centred around a joint control-communication mechanism and a new solution approach. The proposed mechanism incorporates the tracking of the UAV's state within the channel estimation problem to improve it.

D. Notation and Paper Organization

The notation used throughout this paper is outlined in Table I. In Section II, the communication system under consideration and the adopted channel model are described. In Section III, preliminaries on channel estimation in the presence of the beam-squint effect are provided, while Section IV presents the problem considered in this paper along with the description of the proposed channel estimation algorithm. In Section V, the experimental evaluation of the algorithm is included and, finally, the paper's conclusions are drawn in Section VI.

II. SYSTEM AND CHANNEL MODELS

We consider a high-frequency mMIMO point-to-point communication system comprising a terrestrial BS and a UAV user, which are both equipped with UPAs of $N \triangleq N_i \times N_j$ antenna elements each. Without loss of generality, the BS is located at the center $O(x_0, y_0, z_0)$ of the common coordinate system. The UPAs of both the BS and the user are mounted horizontally on the xy plane. This assumption will result into simpler expressions in our analysis, however, a generalisation to the case where the two UPAs are not in parallel is easy to obtain for the reasonable case where the control module of the UAV provides an accurate estimation of its orientation [9].

A. Received Signal Model

The BS implements Orthogonal Frequency Division Multiplexing (OFDM) transmissions with P subcarriers and bandwidth B. To this end, the transmitted signal is represented by the complex-valued $N \times 1$ vector $\mathbf{s}(t,p)$ for time instance t and subcarrier p ($p = 1, 2, \ldots, P$), with $\|\mathbf{s}(t,p)\|_2^2 = 1$. The user is assumed to be equipped with a single reception RF chain where the received signals from all its N antenna elements are combined, thus, realising an analog combiner $\mathbf{f} \in \mathbb{C}^{N\times 1}$, with $|[\mathbf{f}]_n| = 1$ for $n = 1, 2, \ldots, N$. The received signal at the output of the user's single RF chain can be mathematically expressed $\forall t = 1, 2, \ldots, T$ and $\forall p$ as:

$$y(t,p) = \mathbf{f}^{\mathrm{H}}\mathbf{H}(p)\mathbf{s}(t,p) + n_{\mathrm{C}}(t), \tag{1}$$

where $\mathbf{H}(p)$ denotes the complex-valued $N \times N$ channel matrix at each p-th subcarrier and $n_{\mathrm{C}}(t) \sim \mathcal{N}(0, \sigma_{\mathrm{C}}^2)$ represents the Additive White Gaussian Noise (AWGN). We have assumed that the channel remains constant every T time slots and that the AWGN is the same over all P subcarriers per transmission time interval. Note that in the following sections, we omit the subcarrier indexing p in the channel matrix expression $\mathbf{H}(p)$, as the estimation is performed per subcarrier.

In the rest of the paper, we simplify the notation in (1) for the received pilots at each p-th subcarrier by removing the subcarrier index, i.e., we rewrite each received pilot $\mathbf{s}(t)$ as:

$$y(t) = (\mathbf{s}^{\mathrm{T}}(t) \otimes \mathbf{f}^{\mathrm{H}})\mathbf{h} + n_{\mathrm{C}}(t), \tag{2}$$

where $\mathbf{h} \triangleq \mathrm{vec}(\mathbf{H}) \in \mathbb{C}^{N^2\times 1}$. By gathering T time instances with the same beamformer, we build the received vector $\mathbf{y} \triangleq [y(1)\, y(2)\, \cdots\, y(T)]^{\mathrm{T}} \in \mathbb{C}^{T\times 1}$. Thus, the measurement model for channel estimation can be compactly expressed as follows:

$$\mathbf{y} = \mathbf{\Phi}\mathbf{h} + \mathbf{n}_{\mathrm{C}}, \tag{3}$$

where $\mathbf{\Phi} \in \mathbb{C}^{T\times N^2}$ is defined as:

$$\mathbf{\Phi} \triangleq [\mathbf{s}(1) \otimes \mathbf{f}^*\, \mathbf{s}(2) \otimes \mathbf{f}^*\, \cdots\, \mathbf{s}(T) \otimes \mathbf{f}^*]^{\mathrm{T}} \tag{4}$$

$$= [\mathbf{s}(1)\, \mathbf{s}(2)\, \cdots\, \mathbf{s}(T)]^{\mathrm{T}} \otimes \mathbf{f}^{\mathrm{H}} \tag{5}$$

and $\mathbf{n}_{\mathrm{C}} \triangleq [n_{\mathrm{C}}(1)\, n_{\mathrm{C}}(2)\, \cdots\, n_{\mathrm{C}}(T)]^{\mathrm{T}} \in \mathbb{C}^{T\times 1}$.

B. High-Frequency Channel Model With Beam Squint

In cases where the sizes of the BS/UAV UPAs are significantly smaller than the distances between the nodes, i.e., in the far-field regime, the total separation between each k-th BS transmit and each l-th UAV receive antenna ($k, l = 1, 2, \ldots, N$) can be expressed as the sum of the distance from the first transmit antenna to the first receive antenna via each ℓ-th propagation path ($\ell = 1, 2, \ldots, L$), denoted as D_ℓ, and the additional distance attributed to the signal's propagation on the apertures of the BS and UAV antenna arrays, denoted as $d_{\mathrm{TX},\ell}$ and $d_{\mathrm{RX},\ell}$, respectively, yielding the expression:

$$d_{\text{BS-UE},\ell} = D_\ell + d_{\mathrm{TX},\ell} + d_{\mathrm{RX},\ell}. \tag{6}$$

Each $d_{\mathrm{RX},\ell}$ can be expressed as follows [30]:

$$d_{\mathrm{RX},\ell} \triangleq d_0 \sin\theta_{\mathrm{RX},\ell}\left((n_i - 1)\cos\phi_{\mathrm{RX},\ell} + (n_j - 1)\sin\phi_{\mathrm{RX},\ell}\right), \tag{7}$$

where, $d_0 \triangleq \frac{\lambda_c}{2}$ is the antenna separation spacing with $\lambda_c \triangleq \frac{c}{f_c}$ is the carrier wavelength (c: speed of light and f_c: carrier frequency), $\theta_{\mathrm{RX},\ell}, \phi_{\mathrm{RX},\ell} \in [-\pi, \pi]$ are the elevation and azimuth physical angles of arrival, respectively; n_i and n_j denote the planar antenna element index number over the i-th and j-th axes of the common coordinate system. Similarly, we can define $d_{\mathrm{TX},\ell}$ employing the corresponding angles $\theta_{\mathrm{TX},\ell}$ and $\phi_{\mathrm{TX},\ell}$.

Following the geometry-based Rayleigh channel model of L propagation paths, the channel gain between each l-th UAV and k-th BS antenna elements, i.e., each (l,k)-th element of $\mathbf{H}(p)$, is expressed as follows:

$$[\mathbf{H}]_{l,k} = \sum_{\ell=0}^{L-1} \alpha_\ell e^{-\omega D_\ell f_p} e^{-\omega d_{\text{RX},\ell} f_p} e^{-\omega d_{\text{TX},\ell} f_p}, \tag{8}$$

where $\omega \triangleq j2\pi/\lambda_c$, α_ℓ denoting the random complex gain over each ℓ-th propagation path with $\alpha_\ell \sim \mathcal{N}(0, \eta^2_{\alpha_\ell})$, and $f_p \triangleq (1 + p\Delta f/f_c)$ with $\Delta f \triangleq \frac{B}{P}$ indicating the subcarrier separation for M subcarriers and bandwidth B.

For the considered high-frequency communications, the variance of each channel gain α_ℓ depends on the distance $d_{\text{BS-UE},\ell}$ as well as the carrier frequency f_c via the following expression:

$$\eta^2_{\alpha_\ell} \triangleq \frac{P_{\text{TX}} G_0}{L} \frac{1}{d^{\xi_\ell}_{\text{BS-UE},\ell}} e^{-\mathcal{K}(f_c)}, \tag{9}$$

where P_{TX} is the BS transmit power, G_0 is used to capture the antenna gains and depends on the number of antenna elements, ξ_ℓ represents the pathloss exponent and $\mathcal{K}(f)$ is the function of the atmospheric attenuation that depends on the carrier frequency and becomes more severe in THz bands [31].

III. Channel Estimation At High-Frequency Bands

Channel state information can be expressed either in a parametric manner, necessitating the estimation of the spatial parameters of elevation and azimuth Angles-of-Arrival (AoAs) as well as the respective complex channel gains, or non-parametrically, requiring the estimation of the full mMIMO channel matrix. Although parametric approaches demand small training lengths, their performance is significantly deteriorated when multiple propagation paths are present. On the other hand, non-parametric approaches target the estimation of the $N \times N$ mMIMO channel matrix, thus, its N^2 elements are unknowns. Although this number of unknowns can be lowered by exploiting the unique properties of high-frequency channels, such as sparsity, non-parametric approaches still require a significant amount of training symbols.

In the following, we briefly describe the rationale for explicit and parametric channel estimation approaches for high-frequency mMIMO wireless communication systems.

A. Low-Rank Channel Estimation

The estimation of the $N \times N$ channel matrix $\mathbf{H}$ (for each p-th subcarrier used for pilot transmission) via the measurement model in (3) requires the estimation of N^2 unknowns through the N available measurements in vector $\mathbf{y}$. This approach leads to the under-determined channel estimation problem:

$$\mathcal{OP}_1: \min_{\mathbf{H}} \|\mathbf{y} - \mathbf{\Phi h}\|_2^2,$$

which performs unsatisfactorily with fewer than N^2 training symbols. Obviously, for satisfactory performance with large UPAs at the BS and UAV, a massive number of training symbols is required.

To improve upon the previous issue, the inherent low-rank property of $\mathbf{H}$ in high-frequency communication systems can be exploited in the channel estimation formulation [10]. This property indicates that the number of the propagation paths is much lower than the dimensions of the channel matrix, i.e., $L \ll N$ for our case. To this end, the low channel rank constraint can be merged into the channel estimation problem, specifically into the cost function, via the semi-convex nuclear norm, yielding the optimization formulation:

$$\mathcal{OP}_2: \min_{\mathbf{H}} \|\mathbf{H}\|_* + \|\mathbf{y} - \mathbf{\Phi h}\|_2^2,$$

where the nuclear norm is defined for a matrix $\mathbf{X}$ as follows: $\|\mathbf{X}\|_* \triangleq \sum_i q_i(\mathbf{X})$ with $q_i(\mathbf{X})$ being its i-th singular value. This problem can be efficiently solved via the ADMM algorithm [10]. In fact, if one replaces the nuclear norm with the term $\|\mathbf{F}^{\text{H}}\mathbf{H}\mathbf{F}\|_1$ with $\mathbf{F}$ being the $N \times N$ discrete Fourier transform matrix, then the problem becomes an ℓ_1-minimization aiming to exploit the inherited channel sparsity in the beamspace channel representation domain.

B. Parametric Channel Estimation

Capitalizing on the geometric channel model in Section II-B, it suffices to estimate the complex-valued gains and the angles of arrival and departure for all L channel propagation paths to acquire the channel state information. However, this implies that the total number of the resolvable channel paths is known or accurately estimated. This approach is known as parametric channel estimation and includes a much smaller number of unknowns than the N^2 ones considered in the previously described channel estimation approach. Let us use (8) to express the channel matrix for each p-th subcarrier as follows:

$$\mathbf{H} = \sum_{\ell=0}^{L-1} \alpha_\ell e^{-j2\pi v f_c/c} \mathbf{a}_{\text{RX}}(\theta_{\text{RX},\ell}, \phi_{\text{RX},\ell}, p) \mathbf{a}^{\text{H}}_{\text{TX}}(\theta_{\text{TX},\ell}, \phi_{\text{TX},\ell}, p). \tag{10}$$

To estimate the channel parameters, the following optimization problem needs to be solved:

$$\mathcal{OP}_3: \min_{\{\alpha_\ell, \theta_{\text{TX},\ell}, \theta_{\text{RX},\ell}, \phi_{\text{TX},\ell}, \phi_{\text{RX},\ell}\}_{\ell=0}^{L-1}} \|\mathbf{y} - \sum_{\ell=0}^{L-1} (\mathbf{I}_T \otimes \bar{\alpha}_\ell \mathbf{f}^{\text{H}} \times \mathbf{a}_{\text{RX}}(\theta_{\text{RX},\ell}, \phi_{\text{RX},\ell}, p) \mathbf{a}^{\text{H}}_{\text{TX}}(\theta_{\text{TX},\ell}, \phi_{\text{TX},\ell}, p)) \mathbf{s}\|_2, \tag{11}$$

where $\mathbf{a}_{\text{TX}}$ and $\mathbf{a}_{\text{RX}}$ are the steering vectors for the transmitter (TX) and the receiver (RX), respectively. The n-th entry of the TX steering vector is defined as follows:

$$[\mathbf{a}_{\text{TX}}]_n \triangleq e^{-\omega((n_i-1)\sin\theta_{\text{TX},\ell}\cos\phi_{\text{TX},\ell} + (n_j-1)\sin\theta_{\text{TX},\ell}\sin\phi_{\text{TX},\ell})} \tag{12}$$

with $n = 1, 2, \ldots, N$. However, due to its nonlinear nature and sensitivity to even small measurement noise, this problem requires a well-chosen starting point to ensure convergence to a solution [29].

IV. Proposed State-Assisted Channel Estimation

To address the challenge of mMIMO channel estimation with reduced training data, we introduce a novel parametric and non-parametric (hybrid) optimization approach that integrates the state space information from the UAV's control module. Recall

that, the beam-squint effect along with single reception RF chain at the UAV impose a significant challenge when the number of training pilots needs to be limited. It is worth noting that, employing multiple OFDM subcarriers for training becomes impractical when beam squint is present, since, in this case, each subcarrier p encounters a distinct channel matrix $\mathbf{H}(p)$.

A. State-Space Information

Given the limited number of training pilots observed in our scenario, we aim to leverage the space-state information provided by the UAV's controller during the channel estimation process. This approach aligns with recent strategies that integrate control and communications at the physical layer, as highlighted in recent work by Zhao et al. [28]. Furthermore, we extend this concept by establishing a direct two-way link between these modules, enhancing the synergy between control and communication functionalities.

Let the UAV with mass m operate in the 3-Dimensional (3D) space with $\mathbf{p} \in \mathbb{R}^{3\times 1}$, $\dot{\mathbf{p}} \in \mathbb{R}^{3\times 1}$, $\ddot{\mathbf{p}} \in \mathbb{R}^{3\times 1}$ denoting its position, velocity, and acceleration, respectively. These quantities, representing the UAV's state, are actively tracked by its control module using state-vector estimation techniques. To achieve this, the plant (i.e., the physical dynamics model) must first be represented in a suitable format. In this paper, we focus on a double integrator model, whose output is the second integral of its input. This plant is a cornerstone system within motion control applications, describing translational and rotational motion with a single degree of freedom [32]. The mathematical model of the double integrator plant is:

$$\mathbf{x}(k+1) = \mathbf{A}\mathbf{x}(k) + \mathbf{B}\mathbf{u}(k) \in \mathbb{R}^{6\times 1}, \tag{13}$$

where for each control time instant k:

$$\mathbf{A} \triangleq \begin{bmatrix} \mathbf{0}_3 & \mathbf{I}_3 \\ \mathbf{0}_3 & \mathbf{0}_3 \end{bmatrix} \in \mathbb{R}^{6\times 6}, \tag{14}$$

$$\mathbf{B} \triangleq \begin{bmatrix} \mathbf{0}_3^{\mathrm{T}} & \mathsf{m}^{-1}\mathbf{I}_3^{\mathrm{T}} \end{bmatrix}^{\mathrm{T}} \in \mathbb{R}^{6\times 3}, \tag{15}$$

and $\mathbf{u}(k) \in \mathbb{R}^{3\times 1}$ is the control vector related to UAV's acceleration. In addition, the state vector $\mathbf{x}(k)$ is defined as:

$$\mathbf{x}(k) \triangleq \begin{bmatrix} \mathbf{p}(k) & \dot{\mathbf{p}}(k) \end{bmatrix}^{\mathrm{T}} \in \mathbb{R}^{6\times 1},$$

while $\mathbf{x}(k+1)$ represents its derivative, i.e.,

$$\mathbf{x}(k+1) \triangleq \begin{bmatrix} \dot{\mathbf{p}}(k) & \ddot{\mathbf{p}}(k) \end{bmatrix}^{\mathrm{T}} \in \mathbb{R}^{6\times 1}.$$

Let us consider the case where only the position $\mathbf{p}(k)$ is observable. Then, the measurement equation is expressed as:

$$\mathbf{z}(k) = \mathbf{C}\mathbf{x}(k) + \mathbf{n}_{\mathrm{T}}(k) \in \mathbb{R}^{3\times 1}, \tag{16}$$

where

$$\mathbf{C} \triangleq [\mathbf{I}_3, \mathbf{0}_3] \in \mathbb{R}^{3\times 6}, \tag{17}$$

is the measurement matrix and $\mathbf{n}_{\mathrm{T}}(k) \sim \mathcal{N}(\mathbf{0}_3, \sigma_{\mathrm{T}}^2\mathbf{I}_3)$ represents the measurements's AWGN. It is important to highlight that this noise encompasses a range of dynamic disturbances originating from both internal and external factors. Internally, it includes effects such as vehicle jittering and mechanical vibrations. Externally, it arises from environmental influences like wind gusts, turbulence, or other random perturbations, which collectively contribute to small yet unpredictable fluctuations in the UAV's movement [33].

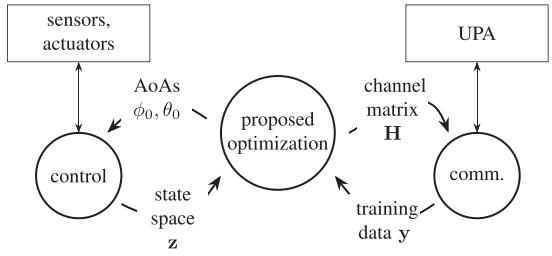

Fig. 1. Data flow diagram of the proposed mMIMO channel approach incorporating the availability of UAV state space.

In Fig. 1, we present the data flow diagram illustrating our proposed approach, showcasing the direct two-way links between the control and communications (comm.) modules. The optimization process is initiated with received training symbols from the communications module, as defined by (3), alongside the state vector containing position/velocity estimations from the UAV's controller, as will described by (16). The outputs of this optimization include the estimated channel matrix, which is subsequently relayed back to the communications module. Additionally, the optimization provides estimations of elevation and azimuth angles of arrival (AoA), enriching the state vector and enhancing observability as part of control unit operations [9].

B. Problem Formulation

The provided state-space information from the UAV controller in (16) measures the vehicle's relative distance from the BS. This distance can be linked with the elevation and azimuth AoAs for the LoS path, namely θ_0 and ϕ_0, are related with according to the following expression [9]:

$$[\cos\phi_0\cos\theta_0, \cos\phi_0\sin\theta_0, \sin\phi_0] = \frac{\mathbf{p}_{\mathrm{UE}}(k) - \mathbf{p}_{\mathrm{BS}}}{\|\mathbf{p}_{\mathrm{UE}}(k) - \mathbf{p}_{\mathrm{BS}}\|_2}, \tag{18}$$

where $\mathbf{p}_{\mathrm{BS}} \in \mathbb{R}^{3\times 1}$ represents the fixed position of the BS, which is reasonably assumed to be perfectly known.

Given that the BS is located at the centre of the global coordinate system, i.e., $\mathbf{p}_{\mathrm{BS}} = \mathbf{0}_3$, the quantity $\mathbf{z}(k)$ represents the BS's distance from the UAV, thus, using (18) yields:

$$\underbrace{[\cos\phi_0\cos\theta_0, \cos\phi_0\sin\theta_0, \sin\phi_0]^{\mathrm{T}}}_{\triangleq \boldsymbol{\xi}(k)} = \underbrace{\frac{\mathbf{z}(k)}{\|\mathbf{z}(k)\|_2}}_{\triangleq \mathbf{b}(k)}, \tag{19}$$

where, to simplify the notations in the subsequent analysis, we introduce the vectors $\boldsymbol{\xi} \in \mathbb{R}^{3\times 1}$ (a nonlinear function of the unknown elevation and azimuth AoAs) and $\mathbf{b} \in \mathbb{R}^{3\times 1}$ the normalized UAV position vector given by the vehicle's control unit measurements.

We will next focus on explicitly estimating the spatial angles related to the LoS path, whereas the angles of the NLoS paths will be incorporated in the estimation of the channel matrix $\mathbf{H}_1$. Thus, we only need to estimate the values of $\theta_{\mathrm{TX},0}$, $\theta_{\mathrm{RX},0}$, $\phi_{\mathrm{TX},0}$,

and $\phi_{\mathrm{RX},0}$. Moreover, when the BS and UAV UPAs are placed in parallel, we have that $\theta_{\mathrm{TX},0} = \theta_{\mathrm{RX},0}$ and $\phi_{\mathrm{TX},0} = \theta_{\mathrm{RX},0}$. Thus, the problem simplifies into the estimation of the angles θ_0 and ϕ_0. Additionally, the consideration of identical UPA antennas in this parallel setup results in identical steering vectors at both the transmitter and receiver, i.e., $\mathbf{a} \triangleq \mathbf{a}_{\mathrm{TX}} = \mathbf{a}_{\mathrm{RX}}$. To this end, one can decompose the mMIMO channel matrix given by (10) into its LoS and NLoS components, yielding the following representation:

$$\mathbf{H} = \underbrace{\bar{\alpha}_0 \mathbf{a}(\theta_0, \phi_0, p)\mathbf{a}^{\mathrm{H}}(\theta_0, \phi_0, p)}_{\triangleq \mathbf{H}_0} + \underbrace{\sum_{\ell=1}^{L-1} \bar{\alpha}_\ell \mathbf{a}(\theta_{\mathrm{TX},\ell}, \phi_{\mathrm{TX},\ell}, p)\mathbf{a}^{\mathrm{H}}(\theta_{\mathrm{TX},\ell}, \phi_{\mathrm{TX},\ell}, p)}_{\triangleq \mathbf{H}_1}, \quad (20)$$

with $\mathrm{rank}(\mathbf{H}_0) = 1$ and $\mathrm{rank}(\mathbf{H}_1) \leq L - 1$.

Putting all above together, we now formulate the proposed *hybrid* optimization problem that combines parametric and non-parametric channel estimation. Our formulation employs the following three objectives which are combined into a weighted cost function:

$$\min_{\alpha_0, \theta_0, \phi_0, \mathbf{H}_1} \|\mathbf{H}_1\|_* + \|\mathbf{y} - \mathbf{\Phi}\mathrm{vec}(\mathbf{H})\|_2^2 + \|\boldsymbol{\xi} - \mathbf{b}\|_2^2$$
$$\text{s.t.} \quad \mathbf{H} = \bar{\alpha}_0 \mathbf{a}\mathbf{a}^{\mathrm{H}} + \mathbf{H}_1. \quad (21)$$

The first objective deals with the rank of the NLoS part of the overall matrix, i.e., $\mathbf{H}_1$. Given that the parameter L (number of non-negligible NLoS components) is typically within $[1, 10]$ [34], the rank of the $N \times N$ matrix $\mathbf{H}_1$ will be low. Utilizing the nuclear norm of the channel matrix eliminates the necessity to know estimate L precisely. Finally, the second objective refers to the least squares' estimation error using the received pilots, while the third one represents the same error from the UAV controller's measurements.

C. ADMM-Based Solution

To solve (21), we adopt an ADMM approach that exhibits favourable convergence properties while being capable to efficiently handle large-scale optimization problems with structured sparsity constraints. To this end, we re-express (21) as follows. The constraint describing the channel structure can be incorporated into the second term in the objective function:

$$\|\mathbf{y} - \mathbf{\Phi}\mathrm{vec}(\mathbf{H})\|_2^2 = \|\mathbf{y} - \mathbf{\Phi}\mathrm{vec}(\mathbf{H}_0 + \mathbf{H}_1))\|_2^2$$
$$= \|\mathbf{y} - \mathbf{\Phi}\mathrm{vec}(\mathbf{H}_0) - \mathbf{\Phi}\mathrm{vec}(\mathbf{H}_1)\|_2^2. \quad (22)$$

Then, following the standard ADMM procedure, we introduce the auxiliary variable $\mathbf{\Omega} \in \mathbb{C}^{N \times N}$ to re-write (21)'s overall cost objective as the sum of independent terms, yielding:

$$\min_{\alpha_0, \theta_0, \phi_0, \mathbf{H}_1, \mathbf{\Omega}} \sum_{i=1}^{3} \mathcal{J}_i \text{ s.t. } \mathbf{H}_1 = \mathbf{\Omega}, \quad (23)$$

where we have introduced the cost functions:

$$\mathcal{J}_1 \triangleq \|\mathbf{H}_1\|_*, \quad (24)$$

$$\mathcal{J}_2 \triangleq \|\mathbf{y} - \bar{\alpha}_0 \mathbf{\Phi}\mathrm{vec}(\mathbf{a}_{\mathrm{RX}}\mathbf{a}_{\mathrm{TX}}^{\mathrm{H}}) - \mathbf{\Phi}\mathrm{vec}(\mathbf{\Omega})\|_2^2, \quad (25)$$

$$\mathcal{J}_3 \triangleq \|\boldsymbol{\xi} - \mathbf{b}\|_2^2. \quad (26)$$

Note that, the introduced variable $\mathbf{\Omega}$ substitutes $\mathbf{H}_1$ in $\mathcal{J}_2$, decomposing the cost function into a sum of three terms involving distinct unknowns. Then, the augmented Lagrangian function is expressed as

$$\mathcal{L}_\rho = \sum_{i=1}^{3} \mathcal{J}_i + \mathtt{Re}\left\{\mathrm{tr}(\mathbf{Z}^{\mathrm{H}}(\mathbf{H}_1 - \mathbf{\Omega}))\right\} + \frac{\rho}{2}\|\mathbf{H}_1 - \mathbf{\Omega}\|_{\mathrm{F}}^2, \quad (27)$$

where $\rho > 0$ represents the dual update step length and $\mathbf{Z} \in \mathbb{C}^{N \times N}$ is the dual variable.

At each i-th ADMM iteration step with $i = 1, 2, \ldots$, the following separate sub-problems need to be solved for the unknown set $\mathcal{X} \triangleq \{\mathbf{H}_1, \mathbf{\Omega}, \theta_0, \phi_0, \alpha_0\}$:

$$\mathcal{X}^{(i+1)} = \arg\min_{\mathcal{X}} \mathcal{L}_\rho \quad (28)$$

$$\mathbf{Z}^{(i+1)} = \mathbf{Z}^{(i)} + \rho(\mathbf{H}_1^{(i+1)} - \mathbf{\Omega}^{(i+1)}) \quad (29)$$

with the following initializations: $\mathbf{Z}^{(1)} = \mathbf{\Omega}^{(1)} = \mathbf{0}_{N \times N}$.

1) Solution for $\mathbf{H}_1$: We remove from $\mathcal{L}_\rho$ the terms which are not affected by $\mathbf{H}_1$, yielding the minimization:

$$\min_{\mathbf{H}_1} \|\mathbf{H}_1\|_* + \mathtt{Re}\left\{\mathrm{tr}\left((\mathbf{Z}^{(i)})^{\mathrm{H}}(\mathbf{H}_1 - \mathbf{\Omega}^{(i)})\right)\right\} + \frac{\rho}{2}\|\mathbf{H}_1 - \mathbf{\Omega}^{(i)}\|^2,$$

which by completing the square, i.e., adding the term $\sqrt{\frac{2}{\rho}}\mathbf{Z}$, the following optimization problem is formulated:

$$\min_{\mathbf{H}_1} \|\mathbf{H}_1\|_* + \frac{2}{\rho}\|\mathbf{H}_1 - \left(\mathbf{\Omega}^{(i)} - \frac{\rho}{2}\mathbf{Z}^{(i)}\right)\|_{\mathrm{F}}^2. \quad (30)$$

This problem is a strictly convex and can be solved via Singular Value Thresholding (SVT) on the matrix $\mathbf{\Omega}^{(i)} - \frac{\rho}{2}\mathbf{Z}^{(i)}$ [35], yielding the iteration:

$$\mathbf{H}_1^{(i+1)} = \mathrm{SVT}_\tau\left(\mathbf{\Omega}^{(i)} - \frac{\rho}{2}\mathbf{Z}^{(i)}\right) \quad (31)$$

with τ being a pre-defined thresholding value that is related with the rank of matrix $\mathbf{H}_1$.

2) Solution for $\mathbf{\Omega}$: Let us first introduce the variable:

$$\boldsymbol{\psi} \triangleq \mathbf{y} - \bar{\alpha}_0^{(i)} \mathbf{\Phi}\mathrm{vec}\left(\mathbf{a}(\theta_0^{(i)}, \phi_0^{(i)})\mathbf{a}^{\mathrm{H}}(\theta_0^{(i)}, \phi_0^{(i)})\right).$$

Then, by removing from $\mathcal{L}_\rho$ the terms being unaffected by $\mathbf{\Omega}$, it leads to the following optimization problem:

$$\min_{\mathbf{\Omega}} \|\boldsymbol{\psi} - \mathbf{\Phi}\mathrm{vec}(\mathbf{\Omega})\|_2^2 + \mathtt{Re}\left\{\mathrm{tr}\left(\mathbf{Z}^{\mathrm{H}}(\mathbf{H}_1^{(i+1)} - \mathbf{\Omega})\right)\right\} + \frac{\rho}{2}\|\mathbf{H}_1^{(i+1)} - \mathbf{\Omega}\|_{\mathrm{F}}^2. \quad (32)$$

Equivalently, by vectorizing the second and third terms and substituting with the vector $\boldsymbol{\omega} \triangleq \mathrm{vec}(\mathbf{\Omega})$:

$$\min_{\boldsymbol{\omega}} \|\boldsymbol{\psi} - \mathbf{\Phi}\boldsymbol{\omega}\|_2^2 - \mathtt{Re}\left\{\mathrm{vec}(\mathbf{Z})^{\mathrm{H}}\boldsymbol{\omega}\right\} + \frac{\rho}{2}\|\mathrm{vec}(\mathbf{H}_1^{(i+1)}) - \boldsymbol{\omega}\|_2^2. \quad (33)$$

This problem can be obtained in closed form by taking the partial derivative over $\boldsymbol{\omega}$, which ends up to:

$$\boldsymbol{\omega}^{(i+1)} = (\boldsymbol{\Phi}^{\mathrm{H}}\boldsymbol{\Phi})^{-1}\left(\boldsymbol{\Phi}\boldsymbol{\psi} + \mathrm{Re}\left\{\mathrm{vec}(\mathbf{Z}^{(i)})\right\} + \frac{\rho}{2}\mathrm{vec}(\mathbf{H}_1^{(i+1)})\right). \tag{34}$$

Finally, the inverse of the vec$(\cdot)$ function needs to be computed to obtain the iteration $\boldsymbol{\Omega}^{(i+1)} = \mathrm{vec}^{-1}(\boldsymbol{\omega}^{(i+1)})$.

3) Solution for α_0: We now focusing on the minimization of the $\mathcal{J}_2$ term:

$$\min_{\alpha_0} \|\mathbf{y} - \bar{\alpha}_0^{(i)}\boldsymbol{\Phi}\mathrm{vec}(\mathbf{a}(\theta_0^{(i)},\phi_0^{(i)})\mathbf{a}^{\mathrm{H}}(\theta_0^{(i)},\phi_0^{(i)})) - \boldsymbol{\Phi}\mathrm{vec}(\mathbf{H}_1)\|_2^2.$$

This problem has the closed-form solution (35) shown at the bottom of this page.

4) Solution for θ_0: By expressing the cost functions $\mathcal{J}_1$ and $\mathcal{J}_2$ via θ_0, the initial problem can be equivalently restated as follows:

$$\min_{\theta_0} \|\mathbf{y} - \bar{\alpha}_0^{(i+1)}\boldsymbol{\Phi}\mathrm{vec}(\mathbf{a}(\theta_0,\phi_0)\mathbf{a}^{\mathrm{H}}(\theta_0,\phi_0) - \boldsymbol{\Phi}\mathrm{vec}(\mathbf{H}_1)\|_2^2 + \|\boldsymbol{\xi}(\theta_0,\phi_0) - \mathbf{b}\|_2^2. \tag{36}$$

The objective of this problem has a non-linear dependence on θ_0, thus, a closed-form solution is not possible. To deal with this, we deploy the iterative Newton's method:

$$\theta_0^{(i)} = \theta_0^{(i)} - \frac{\partial\mathcal{L}}{\partial\theta_0}\Big/\frac{\partial^2\mathcal{L}}{\partial\theta_0^2}, \tag{37}$$

where $\mathcal{L} \triangleq \gamma\mathcal{J}_1 + \mathcal{J}_2$ with $\gamma \in (0,1)$ is a predefined parameter for the weighting between communications and control. Let us define the variable $\boldsymbol{\zeta} \triangleq \mathrm{vec}(\mathbf{a}(\theta_0,\phi_0)\mathbf{a}^{\mathrm{H}}(\theta_0,\phi_0))$. By employing differentiation by parts, yields:

$$\frac{\partial\mathcal{L}}{\partial\theta_0} = \left(\frac{\partial\boldsymbol{\zeta}}{\partial\theta_0}\right)^{\mathrm{T}}\frac{\partial\mathcal{J}_1}{\partial\boldsymbol{\zeta}} + \left(\frac{\partial\boldsymbol{\xi}}{\partial\theta_0}\right)^{\mathrm{T}}\frac{\partial\mathcal{J}_2}{\partial\boldsymbol{\xi}}, \tag{38}$$

where

$$\frac{\partial\boldsymbol{\zeta}}{\partial\theta_0} = \frac{\partial}{\partial\theta_0}\mathrm{vec}(\mathbf{a}\mathbf{a}^{\mathrm{H}}) = \mathrm{vec}\left(\frac{\partial\mathbf{a}}{\partial\theta_0}\mathbf{a}^{\mathrm{H}} + \mathbf{a}\frac{\partial\mathbf{a}^{\mathrm{H}}}{\partial\theta_0}\right) = 2\mathrm{Re}\left\{\mathrm{vec}\left(\frac{\partial\mathbf{a}}{\partial\theta_0}\mathbf{a}^{\mathrm{H}}\right)\right\} = \mathrm{vec}\left((\boldsymbol{\mu}\circ\mathbf{a})\mathbf{a}^{\mathrm{H}}\right).$$

We have used the notations $\boldsymbol{\mu}_\theta \triangleq -j2f_p\pi d_0(\boldsymbol{\mu}_{\theta,1}\otimes\boldsymbol{\mu}_{\theta,2})$ with $\boldsymbol{\mu}_{\theta,1} \triangleq (n_x-1)\cos\theta_0\cos\phi_0$ and $\boldsymbol{\mu}_{\theta,2} \triangleq (n_y-1)\cos\theta_0\sin\phi_0$ for $n_i = 1,2,\ldots,N_i$ and $n_j = 1,2,\ldots,N_j$. Then, it follows:

$$\left(\frac{\partial\boldsymbol{\zeta}}{\partial\theta_0}\right)^{\mathrm{T}}\frac{\partial\mathcal{J}_1}{\partial\boldsymbol{\zeta}} = \mathrm{vec}\left((\boldsymbol{\mu}_\theta\circ\mathbf{a})\mathbf{a}^{\mathrm{H}}\right)^{\mathrm{T}}\boldsymbol{\Phi}^{\mathrm{H}}(\mathbf{g} - \bar{\alpha}_0^{(i+1)}\boldsymbol{\Phi}\boldsymbol{\zeta}). \tag{39}$$

The second part of the derivative (38), which concerns the input $\mathbf{b}$ from the UAV's controller, is given by:

$$\left(\frac{\partial\boldsymbol{\xi}}{\partial\theta_0}\right)^{\mathrm{T}}\frac{\partial\mathcal{J}_2}{\partial\boldsymbol{\xi}} = 2\left[-\cos\phi_0\sin\theta_0, \cos\phi_0\cos\theta_0, 0\right](\boldsymbol{\xi} - \mathbf{b}). \tag{40}$$

Note that, for Newton's method, the following second partial derivative is needed in (37):

$$\frac{\partial^2\mathcal{L}}{\partial\theta_0} = |\bar{\alpha}_0|^2\mathrm{vec}\left((\boldsymbol{\mu}_\theta\circ\mathbf{a})\mathbf{a}^{\mathrm{H}}\right)^{\mathrm{T}}\boldsymbol{\Phi}^{\mathrm{H}}\boldsymbol{\Phi}\mathrm{vec}\left((\boldsymbol{\mu}_\theta\circ\mathbf{a})\mathbf{a}^{\mathrm{H}}\right) \tag{41}$$

5) Solution for ϕ_0: A similar procedure to deriving θ_0 can be followed for the ϕ_0 solution, where the problem:

$$\min_{\phi_0} \|\mathbf{g} - \bar{\alpha}_0^{(i+1)}\boldsymbol{\Phi}\boldsymbol{\zeta}\|_2^2 + \|\boldsymbol{\xi} - \mathbf{b}\|_2^2, \tag{42}$$

can be iteratively solved employing the Newton's step per ADMM iteration, i.e.:

$$\phi_0^{(i)} = \phi_0^{(i)} - \gamma\frac{\partial\mathcal{L}}{\partial\phi_0}\Big/\frac{\partial^2\mathcal{L}}{\partial\phi_0^2}. \tag{43}$$

The first derivative can be calculated as follows:

$$\left(\frac{\partial\boldsymbol{\zeta}}{\partial\phi_0}\right)^{\mathrm{T}}\frac{\partial\mathcal{J}_1}{\partial\boldsymbol{\zeta}} = \mathrm{vec}\left((\boldsymbol{\mu}_\phi\circ\mathbf{a})\mathbf{a}^{\mathrm{H}}\right)^{\mathrm{T}}\boldsymbol{\Phi}^{\mathrm{H}}(\mathbf{g} - \bar{\alpha}_0^{(i+1)}\boldsymbol{\Phi}\boldsymbol{\zeta}), \tag{44}$$

where

$$\boldsymbol{\mu}_\phi \triangleq -j2f_p\pi d_0(\boldsymbol{\mu}_{\phi,1}\otimes\boldsymbol{\mu}_{\phi,2}),$$

with $\boldsymbol{\mu}_{\phi,1} \triangleq -(n_x-1)\sin\theta_0\sin\phi_0$ and $\boldsymbol{\mu}_{\phi,2} \triangleq (n_y-1)\sin\theta_0\cos\phi_0$ for $n_i = 1,2,\ldots,N_i$ and $n_j = 1,2,\ldots,N_j$. Concerning the derivative of the control input part, we have:

$$\left(\frac{\partial\boldsymbol{\xi}}{\partial\phi_0}\right)^{\mathrm{T}}\frac{\partial\mathcal{J}_2}{\partial\boldsymbol{\xi}} = 2\left[-\sin\phi_0\cos\theta_0, -\sin\phi_0\sin\theta_0, \cos(\phi_0)\right](\boldsymbol{\xi} - \mathbf{b}). \tag{45}$$

Finally, the second derivative needed in (43) can be expressed similar to (41) by replacing the vector $\boldsymbol{\mu}_\theta$ with $\boldsymbol{\mu}_\phi$.

D. Complexity Analysis

The proposed hybrid mMIMO channel estimation algorithm applies iteratively the previously described ADMM steps. It terminates after a maximum of $I_{\max}$ iterations, a number considered sufficient for convergence. For analyzing its complexity, we next examine separately each ADMM sub-problem appearing per iteration in Algorithm 1.

Step 1 (line 3) of the proposed ADMM-based solution calls for the solution of (31) which is achieved via SVT, and essentially, the Singular Value Decomposition (SVD) algorithm that requires the calculation of the singular vectors and values of the $N \times N$ matrix $\mathbf{H}_1$. In general, SVD's complexity is of

$$\bar{\alpha}_0 = \frac{\mathrm{vec}\left(\mathbf{a}(\theta_0^{(i)},\phi_0^{(i)})\mathbf{a}^{\mathrm{H}}(\theta_0^{(i)},\phi_0^{(i)})\right)^{\mathrm{H}}(\boldsymbol{\Phi}^{(i)})^{\mathrm{H}}(\mathbf{y} - \boldsymbol{\Phi}\mathrm{vec}(\mathbf{H}_1))}{\mathrm{vec}\left(\mathbf{a}(\theta_0^{(i)},\phi_0^{(i)})\mathbf{a}^{\mathrm{H}}(\theta_0^{(i)},\phi_0^{(i)})\right)^{\mathrm{H}}(\boldsymbol{\Phi}^{(i)})^{\mathrm{H}}\boldsymbol{\Phi}^{(i)}\mathrm{vec}\left(\mathbf{a}(\theta_0^{(i)},\phi_0^{(i)})\mathbf{a}^{\mathrm{H}}(\theta_0^{(i)},\phi_0^{(i)})\right)} \tag{35}$$

Algorithm 1: Proposed State-Assisted Channel Estimation.

Input: $\mathbf{y}$, $\mathbf{s}$, $\mathbf{b}$, ρ, and γ.
Output: $\alpha_0^{(I_{\max})}$, $\theta_0^{(I_{\max})}$, $\phi_0^{(I_{\max})}$, and $\mathbf{H}^{(I_{\max})}$.
1: Initialize $\mathbf{Z}^{(1)} = \mathbf{A}^{(1)} = \mathbf{0}$.
2: **for** $i = 1, 2, \ldots, I_{\max}$ **do**
3: Set $\mathbf{H}^{(i+1)} = \text{SVT}_{\tau_i}(\mathbf{A}^{(i)} - \frac{\rho}{2}\mathbf{Z}^{(i)})$.
4: Obtain $\boldsymbol{\omega}^{(i+1)}$ via (34).
5: Reverse the vectorization function to get $\boldsymbol{\Omega}^{(i+1)}$.
6: Compute $\alpha^{(i+1)}$ using (35).
7: Compute the first and second derivatives in (38) and (41).
8: Update $\theta_0^{(i)}$ using (37).
9: Compute the first and second derivatives in (44) and similar to (41).
10: Update $\phi_0^{(i)}$ using (43).
11: Perform the dual variable update in (29).
12: $\tau_{i+1} = \tau_i/2$
13: **end for**
14: Obtain $\mathbf{H}^{(I_{\max})} = \bar{\alpha}_0^{(I_{\max})}\mathbf{a}_{\text{RX}}(\theta_0^{(I_{\max})}, \phi_0^{(I_{\max})})\mathbf{a}_{\text{TX}}^{\text{H}} + \boldsymbol{\Omega}^{(I_{\max})}$.

the order $\mathcal{O}(N^3)$. To address large-scale problems appearing in mMIMO systems, recent research proposes improvements that exploit parallel processing [36], dropping the complexity order to $\mathcal{O}(N^3/N_{\text{cores}})$, where N_{cores} is the number of the parallel cores.

Step 2 (lines $4-5$) requires inverting the matrix $\boldsymbol{\Phi}^{\text{H}}\boldsymbol{\Phi} \in \mathbb{C}^{N^2\times N^2}$. This inversion has complexity of the order $\mathcal{O}(N^6)$. Fortunately, since matrix $\boldsymbol{\Phi}^{\text{H}}\boldsymbol{\Phi}$ is composed of fixed training symbols (independent of the iterations), its inversion needs to be calculated only once. Additionally, computing (34) involves the derivation of matrix-vector products with a cost of $\mathcal{O}(TN)$; recall that T is the length of the training symbols. Notable, the structure of $\boldsymbol{\Phi}$ allows for more efficient matrix inversion, yielding the derivations:

$$\begin{aligned}(\boldsymbol{\Phi}^{\text{H}}\boldsymbol{\Phi})^{-1} &= \left(([\mathbf{s}(1)\ldots\mathbf{s}(T)]^{\text{T}}\otimes\mathbf{f}^{\text{H}})^{\text{H}}([\mathbf{s}(1)\ldots\mathbf{s}(T)]^{\text{T}}\otimes\mathbf{f}^{\text{H}})\right)^{-1}\\ &= \left(([\mathbf{s}(1)\ldots\mathbf{s}(T)]^{*})[\mathbf{s}(1)\ldots\mathbf{s}(T)]^{\text{T}}\otimes\mathbf{f}\mathbf{f}^{\text{H}}\right)^{-1}\\ &= \left(([\mathbf{s}(1)\ldots\mathbf{s}(T)]^{*})[\mathbf{s}(1)\ldots\mathbf{s}(T)]^{\text{T}}\right)^{-1}\otimes\left(\mathbf{f}\mathbf{f}^{\text{H}}\right)^{-1}.\end{aligned} \tag{46}$$

Following this approach, the inversion of the initial matrix ends up with the inversion of two rank one matrices, which can be derived very efficiently as follows:

$$(\boldsymbol{\Phi}^{\text{H}}\boldsymbol{\Phi})^{-1} = (\bar{\mathbf{S}}\bar{\mathbf{S}}^{\text{H}})^{-1}\otimes\frac{\mathbf{f}\mathbf{f}^{\text{H}}}{(\mathbf{f}^{\text{H}}\mathbf{f})^2}, \tag{47}$$

with $\bar{\mathbf{S}} \triangleq [\mathbf{s}(1)\ldots\mathbf{s}(T)]$. Therefore, the complexity of Step 2 can be reduced to $\mathcal{O}(N^2) + \mathcal{O}(TN)$.

In Steps 3 and 4 (lines $6-11$), the Newton' steps for the angle derivation are included. To reduce computational complexity, we perform only one Newton step per ADMM iteration using a pre-defined step size γ. This simplification primarily involves matrix-vector products. By exploiting Kronecker properties, we can express the product $\boldsymbol{\Phi}^{\text{H}}\boldsymbol{\Phi}$ as vector outer products in (39) and (41), yielding a complexity of the order $\mathcal{O}(N^2)$. Putting all above together, the total complexity order of the proposed channel estimation algorithm is:

$$\mathcal{C}_{\text{total}} = \mathcal{O}(N^3) + 2\mathcal{O}(N^2) + \mathcal{O}(TN). \tag{48}$$

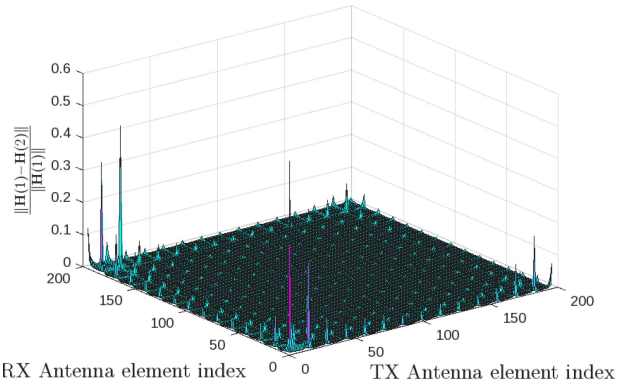

Fig. 2. Example illustration of the differences between two subsequent OFDM subchannels due to frequency selectivity (i.e., the beam-squint effect). The considered 196×196 MIMO system operates at the carrier frequency 150 GHz over a bandwidth of 10 GHz.

V. Numerical Results and Discussion

In this section, we present performance evaluation results for the proposed state-assisted mMIMO channel estimation algorithm, along with comparisons against baseline schemes for both parametric and non-parametric channel estimation. We focus on a symmetric point-to-point system comprising a ground base station (BS) and a UAV. The $N \times N$ channel matrix for each OFDM subcarrier is estimated at the UAV's reception unit after a period of T time instances, during which a certain number of received pilots are collected. The BS transmitter implements fully digital beamforming using N transmission radio frequency (RF) chains.

A. Frequency Selectivity and Training Length

While bandwidth and subcarrier configurations for millimeter-wave (in 5G New Radio's FR2) bands and THz frequencies are not yet standardized, bandwidths ranging from 10 to 30 GHz are generally deemed acceptable for carrier frequencies approaching 100 GHz. Due to this large deployed bandwidth and the possibly large UPAs, each p-th subcarrier (with $p = 1, 2, \ldots, P$) during channel estimation experiences a different channel matrix $\mathbf{H}(p)$. In Fig. 2, we present an example illustration of the normalized difference between the subsequent subcarrier channels $\mathbf{H}(1)$ and $\mathbf{H}(2)$ for the case of an 196×196 MIMO system operating at the carrier frequency 150 GHz over a bandwidth of $B = 10$ GHz. The results demonstrate that even subsequent subcarriers exhibit significant channel differences, necessitating individual channel estimation per subcarrier.

As the UAV moves beyond a distance equivalent to a wavelength, the channel undergoes significant temporal changes, leading to intersymbol interference. For instance, at a carrier

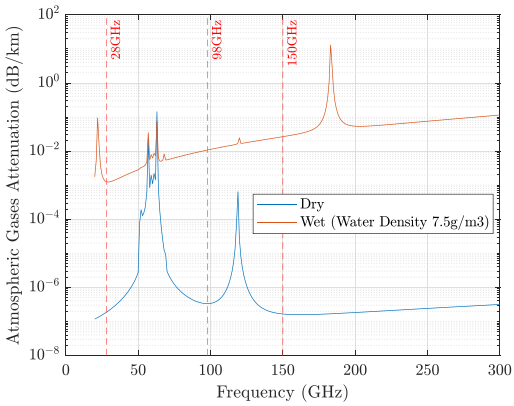

Fig. 3. Atmospheric losses versus the carrier frequency f_c in GHz for a path distance of 100 m, 15 °C of environmental temperature, and atmospheric pressure of 1013.25kPa.

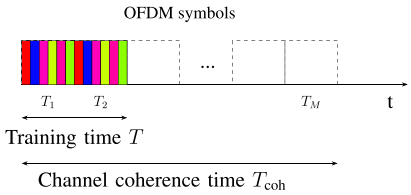

Fig. 4. Consecutive M OFDM symbols within the channel coherence time T_{coh}. Colored slots are used for training data transmissions, while the rest are used for actual data communication.

frequency of 28 GHz, any movement exceeding half of the wavelength ($\frac{\lambda_c}{2} = \frac{c}{2f_c} = 0.0054$ meters or 5.4 millimeters) will cause previous channel estimates to become inaccurate. Similarly, at a carrier frequency of 150 GHz, the minimal distance becomes approximately 0.001 meters. Using this distance and considering typical UAV speeds ranging from 25 to 50 km/h (or $|v| = 36$ km/h or 10 m/s), we can estimate the channel's coherence time. For $f_c = 28$ GHz, the coherence time (T_{coh}) becomes 0.054 seconds, and for $f_c = 150$ GHz, it becomes $0.001/10 = 10^{-4}$ seconds.

Given that each subcarrier experiences a unique channel response among the P subcarriers, it is essential to collect training data consistently from specific subcarriers across consecutive OFDM symbols within the channel's coherence time. However, for training purposes, only a subset of the consecutive OFDM symbols, typically around 20%, will be utilized. To visualize this strategy, we have designed Fig. 4 that includes OFDM symbols with duration T_p for each subcarrier $p = 1, 2, \ldots, P$. Given that M OFDM symbols can be transmitted within the channel coherence time T_{coh}, a portion of these symbols will be designated for training purposes. This subset is visually represented in the figure by colored OFDM symbols, where each color corresponds to a different subcarrier. It is important to clarify that the 20% of the total M OFDM symbols will be allocated for training purposes. The remaining symbols within the coherence time will be utilized for payload transmission.

For vehicle communications, reducing the number of subcarriers is advisable to manage complexity and latency. In our scenario, we adopt a configuration with $P = 200$ subcarriers. Consequently, the duration of each OFDM symbol can be calculated as $T_p = P/B = 10^{-8}$ seconds. Then, we have at most $T_{\text{coh}}/T_p = 10^4$ available OFDM symbols, thus at most $T = 2000$ could be used for the training of each subcarrier. However, in case of mMIMO systems with large antenna array sizes, this upper bound for the training symbols limits the performance of the estimator, especially in terms of achieving satisfactory least-squares performance. Specifically, to recover N^2 parameters within a training duration of $T = 2000$, the antenna array size should bounded to $N \leq \sqrt{T} \approx 45$.

TABLE II
PARAMETERS USED IN THE SIMULATION RESULTS

Carrier Frequency	$f_c = 150$ GHz
Bandwidth	$B = 10$ GHz
Number of multi-paths	$L = 3$
Antenna spacing	$\Delta_c = \lambda_c/2$
Transmit power	$P_{\text{TX}} = 1$ dBW
Antenna gains	$G_0 = 5$ dBi
Number of subcarrier	$P = 200$
Subcarrier spacing	$\Delta f = B/P = 10^8$ Hz
Maximum BS-UAV distance	$5 \leq d_{\text{BS-UE}} \leq 100$ m
Environment temperature	15° C
Atmospheric pressure	101.3 kPa
Path loss exponent	$\xi_0 = 2$, $\xi_\ell = 3$ for $\ell = 1, 2, \ldots, L$
Control unit sampling rate	50 Hz
Maximum number of iterations	$I_{\max} = 50$
Initial SVT threshold value	$\tau_1 = 1$
C&C weighting	$\gamma = 10^{-4}$
ADMM step size	$\rho = 10^{-4}$

B. Simulation Parameters and Setup

The bandwidth of the transmitting channel was set to $B = 10$ GHz with the BS-UAV communication taking place at the carrier frequency $f_c = 150$ GHz. In outdoor applications involving aerial vehicles flying over significant distances from the BS, potential high vapor levels need to be accounted for, which can affect performance. On this premise, the atmospheric attenuation $\mathcal{K}(f_c)$ in our channel model (9) was derived using the MATLAB function $gaspl(\cdot)$ for a wireless link of 100m distance, a temperature of 15 °C, and an atmospheric pressure of 101.3 kPa. In Fig. 3 we plot the losses over f_c for water vapor of 7.5 g/m^3 and for dry air (zero water vapor density). Within the figures, we also highlight with vertical dashed lines potential 5G NR FR2 carrier frequencies, namely, 28 GHz, 98 GHz, and 150 GHz [37]. To mitigate channel losses at the maximum BS-UAV distance of 100 m, the transmit power is set to $P_{\text{TX}} = 1$ dBW. The rest of the parameters used in the simulations for the channel as well as the implementation of Algorithm 1 are included in Table II.

In the following evaluation results, the signal-to-noise ratio is employed, which is defined as:

$$\text{SNR} \triangleq \frac{P_{\text{TX}} G_0}{\sigma_n^2}, \tag{49}$$

where P_{TX} is the BS transmit power, which varies across wireless systems based on application, environment, and regulations. In BS-UAV communication, key factors include free-space path loss and atmospheric attenuation. For cellular BSs (e.g.,

LTE/5G), typical transmit power ranges from -10 dBW to 10 dBW, depending on deployment conditions. Depending on the specific case under investigation, σ_n^2 may represent either the AWGN variance in communication models or the variance in control measurement models.

To evaluate the performance of the proposed algorithm and compare with benchmarks, we have simulated the Mean Squared Error (MSE) weighted over a number R of independent Monte-Carlo (MC) realizations. At each realization, a new channel is observed with randomly selected elevation/azimuth angles of arrival and instantaneous gain for all propagation paths. In particular, the MSE of the mMIMO channel matrix estimation was computed via the following normalized form:

$$\text{MSE} \triangleq \sum_{r=1}^{R} \frac{\|\hat{\mathbf{H}} - \mathbf{H}\|_{\text{F}}^2}{\|\mathbf{H}\|_{\text{F}}^2},$$

where $\hat{\mathbf{H}}$ represents the estimated channel matrix.

The considered baseline schemes are the following:

a) Low-rank and ℓ_1 minimizations using CVX to solve the problems presented in Section III-A, which serve as non-parametric techniques.

b) AoA estimation via MUltiple SIgnal Classification (MUSIC) using second order statistics or perfect channel knowledge (Genie-aided MUSIC). These techniques aim to recover only the LoS elevation and azimuth angles disregarding the NLoS paths.

c) The standard least squares' channel estimation given by:

$$\text{vec}(\hat{\mathbf{H}}_{\text{LS}}) = \mathbf{\Phi}^{\dagger}\mathbf{y}. \tag{50}$$

C. Convergence Behaviour of Algorithm 1

Before evaluating the proposed channel estimation algorithm, we will investigate its convergence behaviour through the evaluation of the MSE for the channel parameter estimation with respect to the number of ADMM iterations $I_{\max}$. We have considered a channel with $L = 3$ propagation paths, and SNR of 20 dB for both control and communication measurements. The distance between the BS and UAV was set to 1m and the water vapor density was set to zero.

In Fig. 5, considering a 49×49 mMIMO channel matrix, the MSE values of the estimations for: the elevation and azimuth angles $\theta^{(i)}$ and $\phi^{(i)}$, respectively, the instantaneous LoS channel gain $\alpha^{(i)}$, the LoS channel matrix $\mathbf{H}_0^{(i)}$ as well as its NLoS part $\mathbf{H}_1^{(i)}$, and the auxiliary variable $\mathbf{\Omega}^{(i)}$ are illustrated. The training data length was set to $T = N = 49$ with a single RF chain. The proposed technique demonstrates exceptional convergence speed across all parameters. Specifically, both $\alpha^{(i)}$ and $\phi^{(i)}$ converge within just two iterations of the ADMM steps. However, it should be noted that reducing the number of training samples T can result in increased convergence errors. Interestingly, this issue can be mitigated by exploiting available information from the UAV's control module. This is illustrated in Fig. 6, where we have considered a 36×36 mMIMO channel matrix with $T = 3N = 108$, with SNR= 20 dB for both control and communication measurements. As shown, when the proposed algorithm is executed without and with control information,

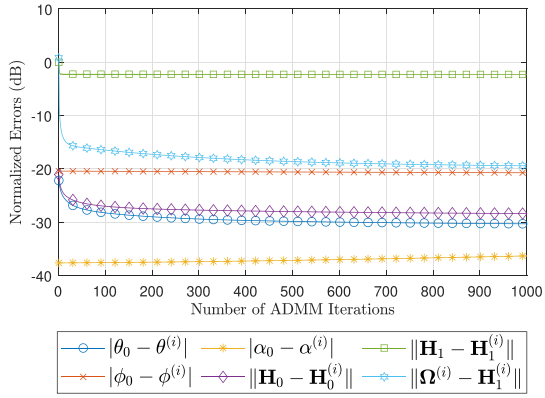

Fig. 5. Convergence behaviour of the proposed Algorithm 1 for estimating the parameters of a 49×49 mMIMO channel matrix using $T = N = 49$ pilots and single RF chain, with SNR= 20 dB for both control and communication measurements, after 1000 Monte-Carlo realizations.

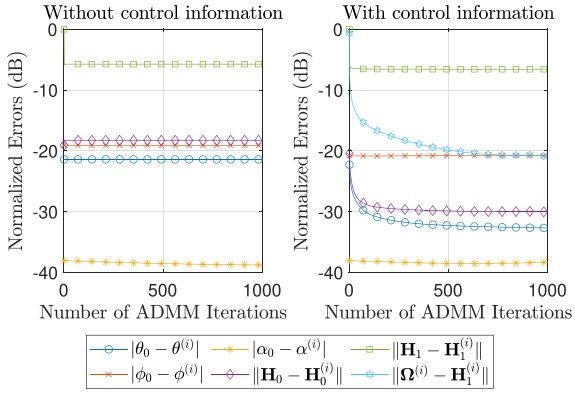

Fig. 6. Convergence behaviour of the proposed Algorithm 1 for estimating the parameters of a 36×36 mMIMO channel matrix using $T = 3N = 108$ pilots, with SNR= 20 dB for both control and communication measurements, after 1000 Monte-Carlo realizations.

the normalized MSE reaches lower levels. Specifically, for the estimation of $\mathbf{H}_0$, the LoS part of the channel, without control information leads to the error of -20 dB, while with control information this errors drops down to -30 dB. It also noted that the normalized errors for the estimation elevation and azimuth AoAs are also significantly reduced when control information is used.

D. Results for the Communication Performance

The normalized MSE performance as a function of the operating SNR in dB for a 36×36 mMIMO channel, considering a UAV with a fully digital combining architecture including $N = 36$ reception RF chains as well as a UAV with a single reception RF chain realizing analog combining, is depicted in Fig. 7. For the case of the 36 RF chains, $T = N = 36$ training instances are necessary to ensure convergence of the non-parametric approaches, such as the least squares, CVX/ℓ_1, and the proposed algorithm. The BS-UAV distance was set as $d_{\text{BS-UE}} = 10$ m and the parameter for the antenna gains as $G_0 = 5$ dBi. As shown in the figure, when the number of the RF chains match the antenna size, the non-parametric estimation schemes exhibit the same MSE values. Due to the presence of

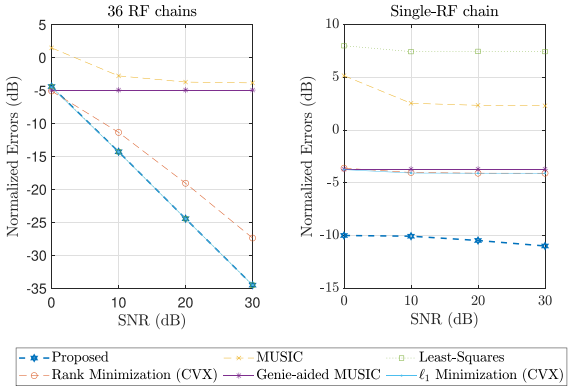

Fig. 7. MSE performance versus the operating SNR in dB for all investigated estimation approaches considering a 36×36 mMIMO channel, $L = 3$ propagation paths, and $T = 3N = 108$ pilot signals.

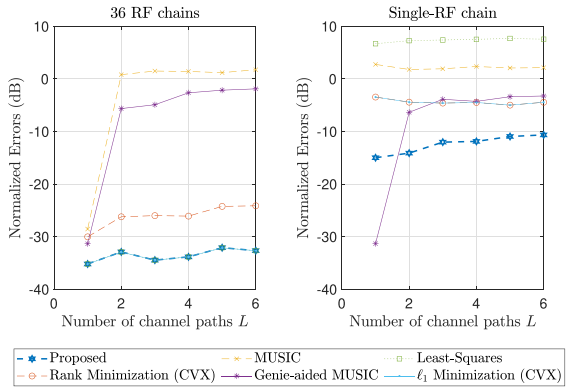

Fig. 8. MSE performance as a function of the number L of multipath channel components for all investigated estimation approaches considering a 36×36 mMIMO channel and $T = 36$ pilot signals. The proposed technique can recover the channel with minimal information from the Single-RF chain while maintaining an acceptable error level.

multipaths, parametric techniques struggle to achieve acceptable performance. Interestingly, for the single RF chain case, the available training length reduces significantly per time instance which impacts all estimation approaches. As observed, the proposed state-space channel estimation technique achieves the best performance, followed by CVX/ℓ_1 techniques that exploit the channel structure. This superiority is attributed to the fact that the proposed method incorporates the UAV's state information into the channel estimation process. In Fig. 8, we plot the normalized MSE over the number of channel paths L. It is demonstrated that, for the case of 36 RF chains, all non-parametric techniques remain unaffected by the value of L, while the parametric ones showcase significant reduction of the MSE with increasing L. When the UAV deploys a single RF chain, the parametric techniques outperform the parametric ones, due to the lack of sufficient number of training data, e.g., $T = 36$. Remarkably, the proposed hybrid channel estimation technique outperforms all the considered baselines for all reduced training cases.

Finally, in Figs. 9 and 10, the achievable rate in Gbits/sec is plotted as a function of the SNR in dB and the training length T, respectively, for all investigated estimation approaches. In both figures, we have considered a 36×36 mMIMO channel, while

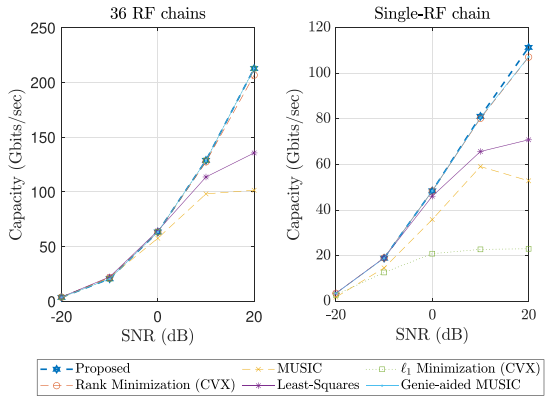

Fig. 9. Achievable rate versus the operating SNR in dB for all investigated estimation approaches considering a 36×36 mMIMO channel, $L = 3$ propagation paths, and $T = N = 36$ pilot signals.

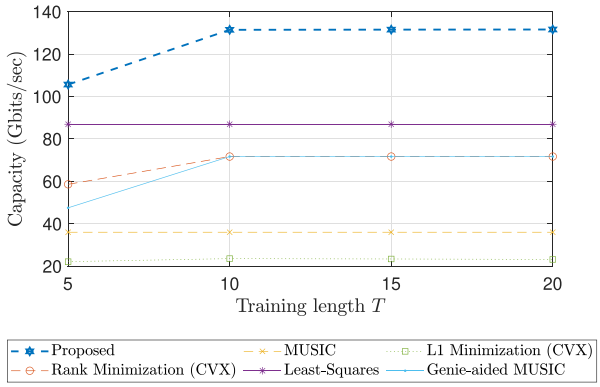

Fig. 10. Achievable rate as a function of the training length T for all investigated estimation approaches considering a 36×36 mMIMO channel with $L = 3$ propagation paths and SNR $= 30$ dB.

in the former, the training length was set as $T = 36$ and for the latter case SNR was set to 30dB. In particular, the rate values were obtained using the formula:

$$C = B \log_2 \left(\det \left(\mathbf{I} + \frac{1}{\sigma_n^2 + \sigma_{\text{CE}}^2} \mathbf{H}\mathbf{H}^{\text{H}} \right) \right), \qquad (51)$$

where $\sigma_{\text{CE}}^2 \triangleq \mathcal{E}\{\frac{\|\hat{\mathbf{H}}-\mathbf{H}\|_F^2}{\|\mathbf{H}\|_F^2}\}$ represents the normalized MSE of channel estimation. As it can observed, for the case of 36 RF chains, all non-parametric approaches exhibit similar performance, while the parametric ones provides smaller rates for SNR values below 0dB. When a single RF chain is used at the UAV, only the parametric techniques and the proposed state-assisted estimation approach retain their data rates. Figure 10 showcases that all non-parametric techniques, including the proposed state-assisted one, converge to the same rate value when T increases. Parametric methods do not exhibit significant improvements with increasing training lengths, often achieving peak data rates with relatively few training data points.

E. Impact of the UAV State Estimation

The measurement vector $\mathbf{z}(k)$ in (16) includes a noisy version of the UAV's state, in our case, the vehicle's position. To remove the noise from this state vector, Kalman filtering is an efficient

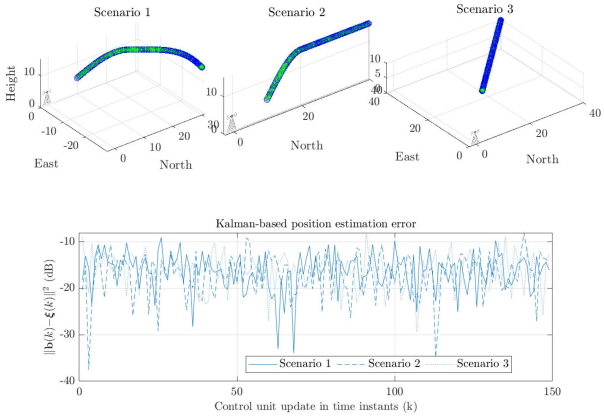

Fig. 11. The three simulated scenarios with UAV trajectories. The blue circles mark the vehicle's true position, while the green stars indicate its position as estimated by the Kalman filter. The evolution of the position estimation error with the implemented Kalman filtering approach is also included. The derived position from the Kalman filter, at each control time instance k, will feed the proposed optimization problem via parameter $\mathbf{b}(k)$ in (19).

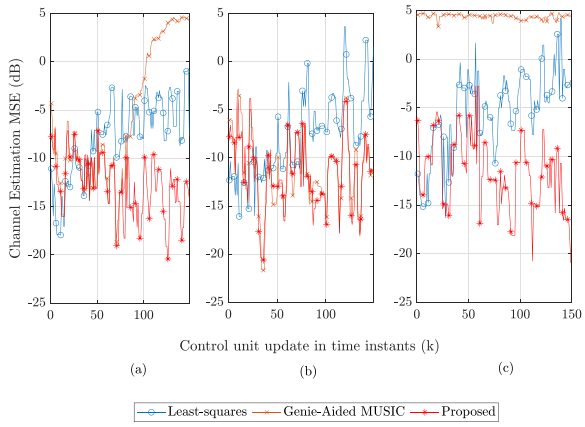

Fig. 12. MSE performance of the estimation of the overall 36×36 mMIMO channel matrix $\mathbf{H}$ versus the control time instants for the different UAV trajectories in Fig. 11: (1) Scenario 1; (1) Scenario 2; and (1) Scenario 3. The proposed channel estimation is able to track the channel at acceptable error levels throughout all three scenarios.

and broadly used approach, given by [38]:

$$\mathbf{x}(k+1) = \underbrace{\mathbf{A}\mathbf{x}(k) + \mathbf{B}\mathbf{u}(k)}_{\text{plant model}} + \underbrace{\mathbf{K}_{\text{ob}}(\mathbf{z}(k) - \mathbf{C}\mathbf{x}(k))}_{\text{correction term}}, \quad (52)$$

where $\mathbf{K}_{\text{ob}}$ represents the observer gain matrix which can be calculated recursively via a Kalman filter; recall that matrices $\mathbf{A}$, $\mathbf{B}$, and $\mathbf{C}$ are defined in (14), (15), and (17), respectively. Clearly, this model for predictive control, consists of two terms, the plant model and a correction term. This term is minimized by the observer gain $\mathbf{K}_{\text{ob}}$, which is defined as [38]:

$$\mathbf{K}_{\text{ob}}(k) \triangleq \mathbf{A}\mathbf{P}(k)\mathbf{C}^{\text{T}}(\sigma_{\text{T}}^2\mathbf{I}_3 + \mathbf{C}\mathbf{P}(k)\mathbf{C}^{\text{T}})^{-1}, \quad (53)$$

where the predicted $(k+1)$-th estimate of the 6×6 covariance matrix $\mathbf{P}(k)$ is:

$$\mathbf{P}(k+1) \triangleq \mathbf{A}\big(\mathbf{P}(k) - \mathbf{P}(k)\mathbf{C}^{\text{T}}(\sigma_{\text{T}}^2\mathbf{I}_3 + \mathbf{C}\mathbf{P}(k)\mathbf{C}^{\text{T}})^{-1}\mathbf{C}\mathbf{P}(k)\big)\mathbf{A}^{\text{T}}, \quad (54)$$

which represents the predicted estimate covariance. It is noted that the state-space model in (13) is free of any form of noise, which is, however, included in the measurement model of (16).

In Fig. 11, three scenarios, each with a different UAV trajectory, are illustrated for $k = 1, 2, \ldots, 150$ time instants. In Scenario 1, the starting point of the UAV is at the point $(0, 10, 5)$ at the same height with the BS's UPA, and the end point at $(-30, 30, 15)$. In Scenario 2, the UAV starts at the point (0,10,5) and stops at the point $(0, 40, 15)$ remaining in the same y-plane, while in Scenario 3, it starts at the point (10,10,10) and stops at $(40, 40, 0)$, remaining in the same z-plane. Note that, the derived position from the Kalman filter, at each control time instance k, will feed the proposed optimization problem via parameter $\mathbf{b}(k)$ in (19). For the three 3D plots at the top of Fig. 11, the blue circles indicate the true UAV position while the green markers resulted from the Kalman-based position estimation via (52).

Given the Kalman-based position estimation, at each control time instance k, the 36×36 mMIMO channel is estimated at the UAV side via the proposed state-assisted approach. The performance evaluation in terms of MSE is shown in Fig. 12,

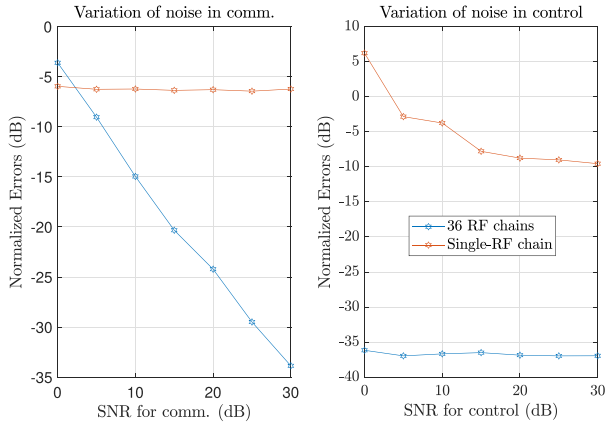

Fig. 13. MSE performance of the proposed estimation of the overall 36×36 mMIMO channel matrix $\mathbf{H}$ for different SNR values for communications (left) and control (right). The single-RF case is significantly impacted by control or communication errors when training is limited to just $T = 36$ symbols.

where the genie-aided MUSIC and the least-squares scheme are also included in the comparisons. As it can be observed from Fig. 12, the proposed technique, that exploits the angles' estimation via the previously described Kalman filtering approach, outperforms all benchmark schemes. Evidently, the MSE of the least squares increases with increasing BS-UAV distance. It is also shown that the performance of the genie-aided MUSIC depends on the specific trajectory scenario. For Scenario 2, genie-aided MUSIC provides similar MSE performance with the proposed approach, whereas, for Scenario 3, it fails to correctly estimate the involved AoAs.

Finally, in Fig. 13, we compare the NMSE of the proposed state-assisted mMIMO channel estimation Algorithm 1 for different SNR levels in the models for communications and control. Specifically, the left subfigure includes the results for the communications model, considering the control noise fixed at 30 dB, whereas the right subfigure presents MSE results for varying control SNR with fixed communication noise at 30 dB. The training length was set to $T = N = 36$, for the single-RF and 36 RF chains. At the left subfigure, the impact

of the communications noise is evaluated, when the control noise is fixed at 30 dB. With 36 RF chains, the impact of the control noise does not affect the channel estimation. However, in the single-RF case, having only $T = 36$ training symbols is insufficient to overcome the control errors.

Considering the impact of the control noise into the channel estimation (Figure 13, right subfigure), it primarily affects the single-RF case. In fact, beyond 30 dB of control SNR, the performance of this case reaches a lower error floor at -12 dB. In contrast, the digital beamforming case is only affected by the noise in the communications model. This is attributed to the fact that the training symbols received with digital beamforming are sufficient to mitigate the effect of noisy UAV position information, thus, improving estimation performance. However, with single-RF, a higher number of training symbols would required to achieve the same error levels. Thus, the limited number of training symbols in the single-RF case imply that the proposed estimation relies more heavily on the additional UAV position information.

VI. Conclusion and Future Work

In this paper, a high-frequency point-to-point communication system between a ground BS and a UAV is considered. Both ends of the mMIMO communication link employed UPAs, the BS realizing fully digital beamforming and the UAV single-RF analog combining, and a wideband multipath channel model was adopted that captures the impact of beam squint at both arrays. A novel hybrid parametric and non-parametric optimization algorithm, building upon ADMM, is proposed to solve the joint control and communication problem, exploiting a direct two-way link between the UAV's control module (for the state vector) and the communication module (for the actual channel estimation). The estimation performance and convergence behaviour of the proposed state-assisted mMIMO channel estimation approach is extensively investigated via simulations over a wideband sub-THz channel, showcasing its superiority over benchmark schemes as well as the interplay of various system parameters. Remarkably, simulation results show that the proposed technique can recover the channel with minimal information from the Single-RF chain while maintaining an acceptable error level.

References

[1] M. Mozaffari, W. Saad, M. Bennis, Y. -H. Nam, and M. Debbah, "A tutorial on UAVs for wireless networks: Applications, challenges, and open problems," *IEEE Commun. Surveys Tut.*, vol. 21, no. 3, pp. 2334–2360, thirdquarter 2019.

[2] M. K. Banafaa et al., "A comprehensive survey on 5G-and-beyond networks with UAVs: Applications, emerging technologies, regulatory aspects, research trends and challenges," *IEEE Access*, vol. 12, pp. 7786–7826, 2024.

[3] C. -X. Wang et al., "On the road to 6G: Visions, requirements, key technologies and testbeds," *IEEE Commun. Surveys Tut.*, vol. 25, no. 2, pp. 905–974, Secondquarter 2023.

[4] I. Valiulahi and C. Masouros, "Multi-UAV deployment for throughput maximization in the presence of co-channel interference," *IEEE Internet Things J.*, vol. 8, no. 5, pp. 3605–3618, Mar. 2021.

[5] Z. Xiao et al., "A survey on millimeter-wave beamforming enabled UAV communications and networking," *IEEE Commun. Surveys Tut.*, vol. 24, no. 1, pp. 557–610, Firstquarter 2022.

[6] B. Wang, F. Gao, S. Jin, H. Lin, and G. Y. Li, "Spatial-and frequency-wideband effects in millimeter-wave massive MIMO systems," *IEEE Trans. Signal Process.*, vol. 66, no. 13, pp. 3393–3406, Jul. 2018.

[7] B. Wang et al., "Spatial-wideband effect in massive MIMO with application in mmWave systems," *IEEE Commun. Mag.*, vol. 56, no. 12, pp. 134–141, Dec. 2018.

[8] M. Wang, F. Gao, S. Jin, and H. Lin, "An overview of enhanced massive MIMO with array signal processing techniques," *IEEE J. Sel. Topics Signal Process.*, vol. 13, no. 5, pp. 886–901, Sep. 2019.

[9] M. Labbadi, Y. Boukal, and M. Cherkaoui, *Advanced Robust Nonlinear Control Approaches for Quadrotor Unmanned Aerial Vehicle*, vol. 384, Berlin, Germany: Springer, 2021.

[10] E. Vlachos, G. C. Alexandropoulos, and J. Thompson, "Wideband MIMO channel estimation for hybrid beamforming millimeter wave systems via random spatial sampling," *IEEE J. Sel. Topics Signal Process.*, vol. 13, no. 5, pp. 1136–1150, Sep. 2019.

[11] G. C. Alexandropoulos, E. Vlachos, and J. Thompson, "Wideband channel tracking for millimeter wave massive MIMO systems with hybrid beamforming reception," in *Proc. IEEE Int. Conf. Acoust., Speech Signal Process.*, 2020, pp. 8698–8702.

[12] B. Wang, M. Jian, F. Gao, G. Y. Li, and H. Lin, "Beam squint and channel estimation for wideband mmWave massive MIMO-OFDM systems," *IEEE Trans. Signal Process.*, vol. 67, no. 23, pp. 5893–5908, Dec. 2019.

[13] M. Jian, F. Gao, Z. Tian, S. Jin, and S. Ma, "Angle-domain aided UL/DL channel estimation for wideband mmWave massive MIMO systems with beam squint," *IEEE Trans. Wireless Commun.*, vol. 18, no. 7, pp. 3515–3527, Jul. 2019.

[14] M. Wang, F. Gao, N. Shlezinger, M. F. Flanagan, and Y. C. Eldar, "A block sparsity based estimator for mmWave massive MIMO channels with beam squint," *IEEE Trans. Signal Process.*, vol. 68, pp. 49–64, 2020.

[15] G. C. Alexandropoulos, E. Vlachos, and B. Smida, "Localization and channel estimation for UAV-assisted millimeter wave communications," in *Proc. 54th Asilomar Conf. Signals, Syst., Comput.*, Pacific Grove, CA, USA, 2020, pp. 1318–1322.

[16] J. He, A. Fakhreddine, and G. C. Alexandropoulos, "Joint channel and direction estimation for ground-to-UAV communications enabled by a simultaneous reflecting and sensing RIS," in *Proc. IEEE Int. Conf. Acoust., Speech Signal Process.*, Rhodes, Greece, 2023, pp. 1–5.

[17] H. Yu, P. Guan, Y. Wang, and Y. Zhao, "Spatial spectrum-based channel estimation for wideband mmWave system with beam squint," *IEEE Access*, vol. 9, pp. 16164–16172, 2021.

[18] Y. Lin, S. Jin, M. Matthaiou, and X. You, "Tensor-based channel estimation for millimeter wave MIMO-OFDM with dual-wideband effects," *IEEE Trans. Commun.*, vol. 68, no. 7, pp. 4218–4232, Jul. 2020.

[19] Y. Byun, H. Kim, S. Kim, and B. Shim, "Channel estimation and phase shift control for UAV-carried RIS communication systems," *IEEE Trans. Veh. Technol.*, vol. 72, no. 10, pp. 13695–13700, Oct., 2023.

[20] E. Basar et al., "Reconfigurable intelligent surfaces for 6G: Emerging hardware architectures, applications, and open challenges," *IEEE Trans. Veh. Technol. Mag.*, vol. 19, no. 3, pp. 27–47, 2024, doi: 10.1109/MVT.2024.3415570.

[21] Y. Zhang, M. El-Hajjar, and L.-l. Yang, "Multi-layer sparse Bayesian learning for mmwave channel estimation," *IEEE Trans. Veh. Technol.*, vol. 73, no. 3, pp. 3485–3498, Mar., 2024.

[22] S. Uchimura, K. Ishibashi, H. Iimori, P. V. Klaine, and S. Malomsoky, "Efficient channel tracking based on compressive sensing for OFDM millimeter-wave systems," *IEEE Trans. Veh. Technol.*, vol. 73, no. 8, pp. 11411–11426, Aug., 2024.

[23] J. Zhao, J. Liu, F. Gao, W. Jia, and W. Zhang, "Gridless compressed sensing based channel estimation for UAV wideband communications with beam squint," *IEEE Trans. Veh. Technol.*, vol. 70, no. 10, pp. 10265–10277, Oct. 2021.

[24] E. Vlachos, C. Mavrokefalidis, and K. Berberidis, "Channel estimation for UAV-based mmwave massive MIMO communications with beam squint," in *Proc. 30th Eur. Signal Process. Conf.*, 2022, pp. 1696–1700.

[25] R. Zhang, L. Cheng, S. Wang, Y. Lou, W. Wu, and D. W. K. Ng, "Tensor decomposition-based channel estimation for hybrid mmWave massive MIMO in high-mobility scenarios," *IEEE Trans. Commun.*, vol. 70, no. 9, pp. 6325–6340, Sep. 2022.

[26] S. Javaid et al., "Communication and control in collaborative UAVs: Recent advances and future trends," *IEEE Trans. Intell. Transp. Syst.*, vol. 24, no. 6, pp. 5719–5739, Jun., 2023.

[27] J. Zhao, F. Gao, L. Kuang, Q. Wu, and W. Jia, "Channel tracking with flight control system for UAV mmWave MIMO communications," *IEEE Commun. Lett.*, vol. 22, no. 6, pp. 1224–1227, Jun. 2018.

[28] J. Zhao, F. Gao, G. Ding, T. Zhang, W. Jia, and A. Nallanathan, "Integrating communications and control for UAV systems: Opportunities and challenges," *IEEE Access*, vol. 6, pp. 67519–67527, 2018.
[29] E. Vlachos, C. Mavrokefalidis, and K. Berberidis, "Velocity-aided channel estimation for spatially selective mmwave massive MIMO communications," in *Proc. 31st Eur. Signal Process. Conf.*, 2023, pp. 1455–1459.
[30] K. Dovelos, M. Matthaiou, H. Q. Ngo, and B. Bellalta, "Channel estimation and hybrid combining for wideband terahertz massive MIMO systems," *IEEE J. Sel. Areas Commun.*, vol. 39, no. 6, pp. 1604–1620, Jun. 2021.
[31] J. M. Jornet and I. F. Akyildiz, "Channel modeling and capacity analysis for electromagnetic wireless nanonetworks in the terahertz band," *IEEE Trans. Wireless Commun.*, vol. 10, no. 10, pp. 3211–3221, Oct. 2011.
[32] V. G. Rao and D. S. Bernstein, "Naive control of the double integrator," *IEEE Control Syst. Mag.*, vol. 21, no. 5, pp. 86–97, Oct. 2001.
[33] R. Zhang, W. Wu, X. Chen, Z. Gao, and Y. Cai, "Terahertz integrated sensing and communication-empowered UAVs in 6G: A transceiver design perspective," *IEEE Veh. Technol. Mag.*, early access, Feb., 17, 2025, doi: 10.1109/MVT.2025.3531088.
[34] T. S. Rappaport, R. W. Heath Jr, R. C. Daniels, and J. N. Murdock, *Millimeter Wave Wireless Communications*, London, U.K.: Pearson Education, 2015.
[35] J. -F. Cai, E. J. Candes, and Z. Shen, "A singular value thresholding algorithm for matrix completion," *SIAM J. Optim.*, vol. 20, no. 4, pp. 1956–1982, 2010.
[36] P. Nobel, E. Candès, and S. Boyd, "Tractable evaluation of stein's unbiased risk estimate with convex regularizers," *IEEE Trans. Signal Process.*, vol. 71, pp. 4330–4341, 2023.
[37] Electronic Communications Committee (ECC), "The European table of frequency allocations and applications in the frequency range 8.3 KHz to 3000 GHz," Eur. Conf. Postal Telecommun. Admin. (CEPT), Copenhagen, Tech. Rep., 2023. [Online]. Available: https://docdb.cept.org/download/4316
[38] L. Wang, *Model Predictive Control System Design and Implementation Using MATLAB*, vol. 3, London, U.K.: Springer, 2009.

Evangelos Vlachos (Member, IEEE) received the Diploma in computer engineering and informatics, the M.Sc. degree in signal processing and telecommunications, and the Ph.D. degree in signal processing for wireless communications from the University of Patras (UoP), Patras, Greece, in 2005, 2009, and 2015, respectively. From 2015 to 2016, he was a Postdoctoral Researcher with the Laboratory of Signal Processing and Telecommunications in Computer Engineering and Informatics, UoP, working on distributed signal processing over networks. In 2016 2016, he was a Postdoctoral Researcher with Visualization and Virtual Reality Group, UoP, on graph signal processing. From 2017 to 2019, he was a Postdoctoral Researcher in signal processing for communications currently working at the Institute for Digital Communications (IDCOM), University of Edinburgh. In 2019 was elected Research Associate at Industrial Systems Institute, "ATHENA" Research Centre. His research interests include wireless communications, machine learning and optimization, adaptive control, and filtering algorithms.

Christos Mavrokefalidis (Member, IEEE) received the Diploma in computer engineering and informatics, the master's degree in signal processing systems, and the Ph.D. degree in signal processing for wireless communications, from the University of Patras, Patras, Greece, in 2004, 2006, and 2011, respectively. Since 2006, he has been a Research Associate with the Signal Processing and Communications Laboratory of the Computer Engineering and Informatics Department, University of Patras. Since 2019, he has also been with the Multimedia Information Processing Systems Group of the Industrial Systems Institute, Athena Research Center, Patras. His research interests include statistical signal processing and learning with a focus on estimation theory, adaptive/distributed signal processing, and sparse representations. He was involved in the design of integrated circuits for microprocessors that support multimedia operations. He has been also involved in numerous national, European and bilateral research projects in application areas like wireless communications and sensor networks, smartgrids, and computer vision. Dr. Christos Mavrokefalidis is a Regular Reviewer in various journals and conferences in the general area of signal processing. He is a member of the Technical Chamber of Greece.

Kostas Berberidis (Senior Member, IEEE) From 2008 till recently, he was the Director of the Signal Processing & Communications Research Unit, Computer Technology Institute and Press "Diophantus". Since 2018, he has been a Collaborating Faculty with the Industrial Systems Institute, Athena Research Center, Greece. He is currently a Professor with the Computer Engineering and Informatics Department, University of Patras, Patras, Greece, and the Head of the Signal Processing and Communications Laboratory. His research interests include distributed signal and information processing and learning, adaptive learning algorithms, signal processing for communications, wireless communications and sensor networks, and array signal processing. Prof. Berberidis was/is a Member of scientific and organizing committees of several international conferences, including most recent EUSIPCO-2022 (TPC Co-Chair) and the IEEE ICASSP-2023 (General Co-Chair). He was also an Associate Editor for the IEEE TRANSACTIONS ON SIGNAL PROCESSING and IEEE SIGNAL PROCESSING LETTERS, the Guest Editor of the *EURASIP Journal on Advances in Signal Processing*, and an Associate Editor for the *EURASIP Journal on Advances in Signal Processing*. From 2010 to 2017, he was the Chair of the Greece Chapter of the IEEE Signal Processing Society. He was a Member of the IEEE SPS "Signal Processing Theory and Methods" Technical Committee, IEEE COMSOC "Signal Processing for Communications and Electronics" Technical Committee, and EURASIP Special Area Team "Theoretical and Methodological Trends for Signal Processing". He was a Member of the Board of the Directors (BoD) of EURASIP for two concecutive terms from 2017 to 2023. Since 2015, he is a Member of the EURASIP Technical Area Committee "Signal Processing for Multisensor Systems". He is a Member of the Technical.

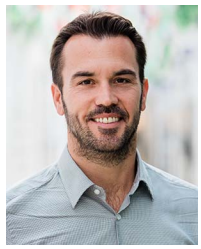

George C. Alexandropoulos (Senior Member, IEEE) received the Diploma (Integrated M.Sc.) in engineering, and the M.A.Sc. and Ph.D. degrees in computer engineering and informatics from the School of Engineering, University of Patras, Greece, in 2003, 2005, and 2010, respectively. He has held senior research positions with various Greek universities and research institutes, and was a Senior Research Engineer and the Principal Researcher with the Mathematical and Algorithmic Sciences Lab, Paris Research Center, Huawei Technologies, France, and Technology Innovation Institute, Abu Dhabi, UAE, respectively. He is currently an Associate Professor with the Department of Informatics and Telecommunications, School of Sciences, National and Kapodistrian University of Athens (NKUA), Athens, Greece, and an Adjunct Professor with the Department of Electrical and Computer Engineering, University of Illinois Chicago, Chicago, IL, USA. His research interests include algorithmic design and performance analysis for wireless networks with emphasis on multi-antenna transceiver hardware architectures, full duplex MIMO, active and passive RISs, ISAC, millimeter wave and THz communications, as well as distributed machine learning algorithms. He is the Editor of IEEE TRANSACTIONS ON COMMUNICATIONS, IEEE TRANSACTIONS ON GREEN COMMUNICATIONS AND NETWORKING, IEEE WIRELESS COMMUNICATIONS LETTERS, *Frontiers in Communications and Networks*, and *ITU Journal on Future and Evolving Technologies*. Dr. Alexandropoulos is a Senior Member of the IEEE Communications, Signal Processing, Vehicular Technology, and Information Theory Societies, the Chair of the EURASIP Technical Area Committee on Signal Processing for Communications and Networking, as well as a registered Professional Engineer of the Technical Chamber of Greece. From 2022 to 2024, he was a Distinguished Lecturer of the IEEE Communications Society. He has participated and/or technically managed more than 15 European Union, international, and Greek research, innovation, and development projects, including the H2020 RISE6G, SNS JU TERRAMETA, SNS JU 6G-DISAC, and ESA PRISM projects dealing with RIS-empowered smart wireless environments, THz RISs, distributed ISAC, and RIS demonstration for localization and mapping, respectively. He was the recipient of the best Ph.D. thesis award in 2010, IEEE Communications Society Best Young Professional in Industry Award 2018, EURASIP Best Paper Award of the Journal on Wireless Communications and Networking 2021, IEEE Marconi Prize Paper Award in Wireless Communications 2021, Best Paper Award from the IEEE GLOBECOM 2021, IEEE Communications Society Fred Ellersick Prizes 2023 and 2024, IEEE Communications Society Leonard G. Abraham Prize 2024, and NKUA's Research Excellence Award for the academic year from 2023 to 2024. More information is available at www.alexandropoulos.info.